Available online at www.eccomasproceedia.org
Eccomas Proceedia SMART (2023) 1053-1064

ECCOMAS
Proceedia

X ECCOMAS Thematic Conference on Smart Structures and Materials
SMART 2023
D.A. Saravanos, A. Benjeddou, N. Chrysochoidis and T. Theodosiou (Eds)

DYNAMIC STRAIN VERSUS ACCELERATION BASED ROBUST STRUCTURAL HEALTH MONITORING FOR A POPULATION OF COMPOSITE AEROSTRUCTURES UNDER UNCERTAINTY

FATION T. FERA*, IOANNIS E. SARAMANTAS*, PANAYOTIS E. SPILIOTOPOULOS*, YOAV OFIR†, IDDO KRESSEL†, SPILIOS D. FASSOIS*, JOHN S. SAKELLARIOU*, MOSHE TUR§, CHRISTOS SPANDONIDIS‡

*Stochastic Mechanical Systems and Automation (SMSA) Laboratory
University of Patras, 26504 Patras, Greece
e-mail: fationfera@upnet.gr (FTF), jsar@upnet.gr (IES), p.spiliotop@upnet.gr (PES)
fassois@upatras.gr (SDF), sakj@upatras.gr (JSS)

†Advanced Structural Technologies, Engineering and Development Center, Aviation Group,
Israel Aerospace Industries (IAI)
Ben Gurion International Airport, 70100, Israel
e-mail: yoaofir@iai.co.il (YO), ikressel@iai.co.il (IK)

§Tel Aviv University
Ramat Aviv 69978, Israel
e-mail: tur@tauex.tau.ac.il (MT)

‡Prisma Electronics S.A.
87 Dimokratias Avenue, 68100, Alexandroupolis, Greece
e-mail: c.spandonidis@prismael.com (CS)

Key words: Robust SHM, Population-based SHM, Dynamic Strain, Composite Structures

Abstract. The study explores the use of dynamic strain signals for Structural Health Monitoring (SHM) in a population of composite aerostructures under uncertainty. Both delamination and debonding type damage, of two minor levels and occurring at two distinct locations, are considered. Two robust damage detection methods, based on Multiple Model and Hyper-Sphere type approximations of the healthy subspace, are employed using Multiple-Input Single-Output Transmittance Functions for eliminating excitation profile variability effects. Robust damage characterization is based on an hierarchical Multiple Model based framework. The results of the study, based on thousands of Monte Carlo simulations under various uncertainty factors, indicate that population wide damage diagnosis can be effectively carried out based on dynamic strain signals, although the use of vibration acceleration signals offers an edge in performance, in particular for 'low' level damage detection and for damage characterization.

Peer-review under responsibility of the organizing committee of SMART 2023.
doi: 10.7712/150123.9856.448208

1 INTRODUCTION

The study focuses on exploring the potential of dynamic strain signals for effective damage diagnosis (detection and characterization) for a population of composite aerostructures under non-observable excitation. Particular emphasis is placed on systematic performance assessment under the detrimental effects of uncertainty, including population, temperature, and unobservable force excitation uncertainty which necessitate the use of *robust to uncertainty* methods, as well to comparisons with the performance achieved by vibration acceleration signals.

The practical importance of the study stems from the fact that composite structures are increasingly employed in the aerospace industry, with damage diagnosis / Structural Health Monitoring (SHM) gaining importance. Moreover, the detrimental effects of uncertainty on diagnostic performance are well known, along with the obvious unavailability of the excitation forces acting during flight.

The use of dynamic strain signals for damage diagnosis has gained popularity in recent years [1, 2, 3, 4, 5, 6]. In [1] the presence of damage is revealed by discrepancies in Frequency Response Functions (FRFs), with strain FRFs reportedly exhibiting an increased sensitivity to damage over their acceleration counterparts. In [2] a strain-based damage index independent of the excitation is introduced. In an exhaustive study focused on a metallic beam [3] with the use of the modal assurance criterion and modal vector error, the superiority of dynamic strain based damage diagnosis over its acceleration based counterpart is reported. Damage diagnosis (detection and characterization) in composite aerostructures via strain measurements and Support Vector Machines is reported in [4] with classification efficiency reaching 99.3%, while the use of Convolutional Neural Networks for accounting for excitation variability is reported in [5] with high achievable accuracy (99% for detection and 83% for localization) as well. Very good results (detection accuracy of 98.1%) are also reported in [6] for strain-based damage detection in aerostructures via the use of clustering accounting for excitation variability.

Despite the progress achieved so far, dynamic strain based damage diagnosis effectiveness for composite aerostructures under population and a combination of other uncertainty factors remains a highly important research topic. The unique points of focus and original contributions of the present study within this context may be summarized as follows: (i) Systematic and comprehensive exploration of the effectiveness of dynamic strain based damage diagnosis under considerable population, excitation profile, and temperature uncertainty. (ii) Determination of the achievable performance limits for robust diagnosis, including detection and (type, location, and size) characterization. (iii) Comparative assessment of the dynamic strain based achievable performance with its vibration acceleration based counterpart as reported in our companion paper [7].

The study is based on thousands of Monte Carlo numerical experiments with a population of beam-like composite structures simulated using perturbations of a Finite Element Model (FEM) developed under the Greece-Israel Bilateral Cooperation project REALISM and considering damage at two distinct locations and of two potential levels (see our companion paper [7]). Experimental results are also presented in a parallel study [8]. Statistical time series type unsupervised robust damage detection and supervised robust damage characterization methods are utilized based on Multiple Model (MM) and Hyper-Sphere (HS) methods [9, 10]. They all use Multiple-Input Single-Output Transmittance Function (MISO-TF) representations of the

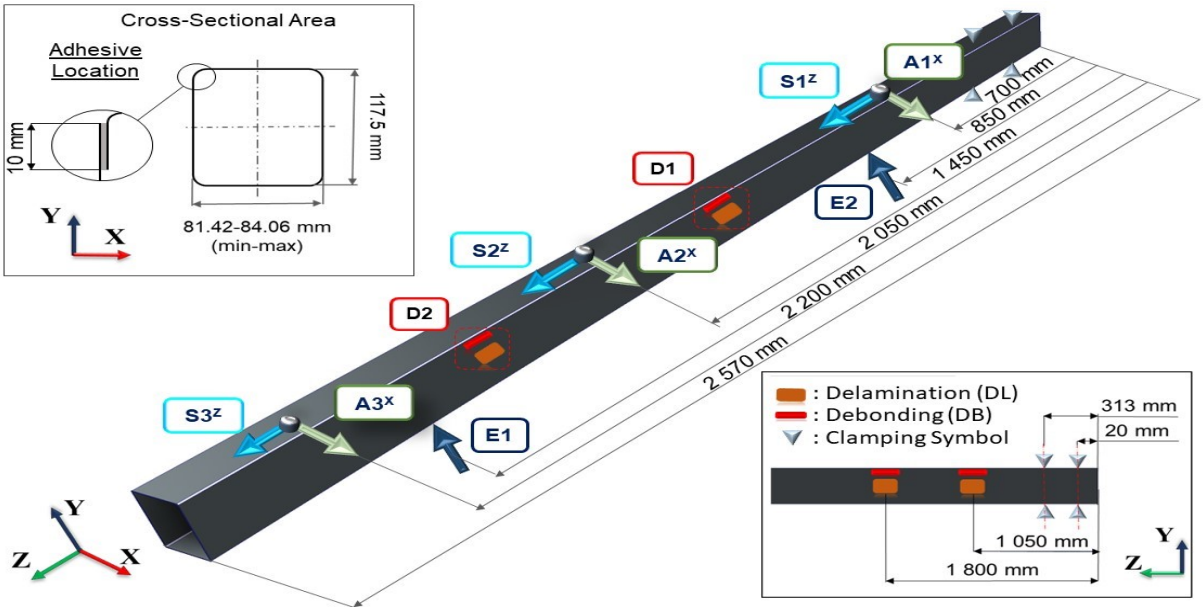

Figure 1: Schematic representation of the nominal composite aerostructure, indicating the damage locations (red/orange rectangle for debonding/delamination, respectively), excitation locations (dark blue arrows), and the sensor locations with measurement directions (green for the accelerometers, turquoise for the strain gauges). The indicated clamping upper nodes (along the center line) are symmetrical with the lower nodes with respect to the Z-X plane. (All dimensions in mm.)

dynamics for eliminating excitation profile effects, and Principal Component Analysis (PCA) based feature transformation and reduction. Compared to typical Machine Learning type methods, an important advantage of the aforementioned approaches is the use of a limited number of numerical experiments in their Baseline/Learning Phase.

2 THE FINITE ELEMENT MODEL, THE UNCERTAINTY FACTORS, AND THE DAMAGE SCENARIOS

2.1 The Finite Element model

The aerostructure considered is a 2 570 mm long (nominal length) composite beam schematically depicted in Figure 1. It consists of the web, characterized by a $[0/45_2/0/45/0]_S$ architecture, and the skin, characterized by various Carbon Epoxy plies along its length. Adhesive is used in the assembly, yielding a rectangular 82.74 ($\pm$1.32) $\times$ 117.5 mm cross-section hollow beam. Details on the *nominal* values of the material properties under the *nominal* temperature of 25° C are presented in Table 1.

The aerostructure is modeled via a Finite Element Model (FEM), presented in detail in our companion paper [7] and implemented in Abaqus® 6.14 using shell and brick elements with a mesh size of 5×5.136 mm and $5 \times 0.2 \times 0.588$ mm, respectively. The beam is clamped at one end (node translations in all directions are constrained) and is excited at two locations E1 and E2 along the Y-axis via two band-limited stochastic force profiles. Measurements at three locations of both dynamic strain ($S1^Z$, $S2^Z$, $S3^Z$) along the Z-axis and vibration acceleration ($A1^X$, $A2^X$,

Properties	Carbon Epoxy (Web/Skin) (Shell Elements)		Adhesive (3-D Brick Elements)	
	Nominal Value	Delamination (Reduction)[1]	Nominal Value	Debonding (Reduction)
Young's Modulus E11 (Pa)	5.78×10^{10}	20%	1.02×10^{10}	99.9%
Young's Modulus E22 (Pa)	5.60×10^{10}	60%	1.02×10^{10}	99.9%
Shear Modulus G12 (Pa)	3.87×10^{10}	60%	3.93×10^{8}	0%
Poisson's ratio ν	0.07	0%	0.30	0%
Density ρ (kg/m^3)	1 490	0%	1 900	100%

Beam Length: 2 570 mm; Total number of FEM nodes: 150 383; Total number of FEM elements: 187 098.
[1]Percentage reduction from nominal values in the damaged (affected) area.

Table 1: Material properties of the nominal composite aerostructure under the healthy and damaged states.

A3^X) along the X-axis, are made; see Figure 1.

Modal analysis and response calculations are based on the Abaqus® modal dynamic analysis using modal superposition. The modal analysis is preceded by natural frequency extraction within the $0 - 2\,000$ Hz range (bandwidth of interest) using the Block-Lanczos method. The integration time step is selected equal to 2.5×10^{-4} s ($f_{int} = 40$ kHz) and 100 000-sample long signals are obtained. These are subsequently re-sampled within Abaqus®, resulting in $N = 10\,000$-sample long signals sampled at $f_s = 4$ kHz.

2.2 The uncertainty factors

The uncertainty factors are related to the population, on one hand, and the Environmental and Operational Conditions (EOCs) on the other. A summary is provided in Table 2. Population uncertainty mainly stems from manufacturing and material uncertainty, and is presently distinguished into Skin Variability (SV) and Adhesive Variability (AV). Each one is modeled via random sampling from three uniform distributions corresponding to material property deviations from their nominal values within the $[-10\%, -8\%]$, $[-1\%, +1\%]$, and $[+8\%, +10\%]$ ranges (each time a common sample for skin E11, E22, G12 and a sample for adhesive G12 are used).

Uncertainty	*Range*
Skin Variation[1]	$SV \sim \mathcal{U}[(-10,-8),(-1,+1),(+8,+10)]$ %
Adhesive Variation[2]	$AV \sim \mathcal{U}[(-10,-8),(-1,+1),(+8,+10)]$ %
Temperature[3]	$T_I \sim \mathcal{U}[(-50,-40),\ldots,(-10,0),(0,10),\ldots,(60,70)]$ °C
	$T_{II} \sim \mathcal{U}[(-50,-38),\ldots,(-26,-14),(-14,-2),\ldots,(58,70)]$ °C

[1]Variation of E11, E22, G12 from their nominal values. [2]Variation of G12 from its nominal value.
[3]T_I/T_{II}: Temperature ranges in the Baseline/Inspection Phase, respectively (in each simulation a single temperature is randomly selected from one of the indicated uniform distributions $\mathcal{U}(\cdot,\cdot)$); T_I and T_{II} created with a step of 12°C and 10°C, respectively, from −50°C to 70°C (12/10 uniform distributions in T_I/T_{II}).

Table 2: The considered uncertainty factors.

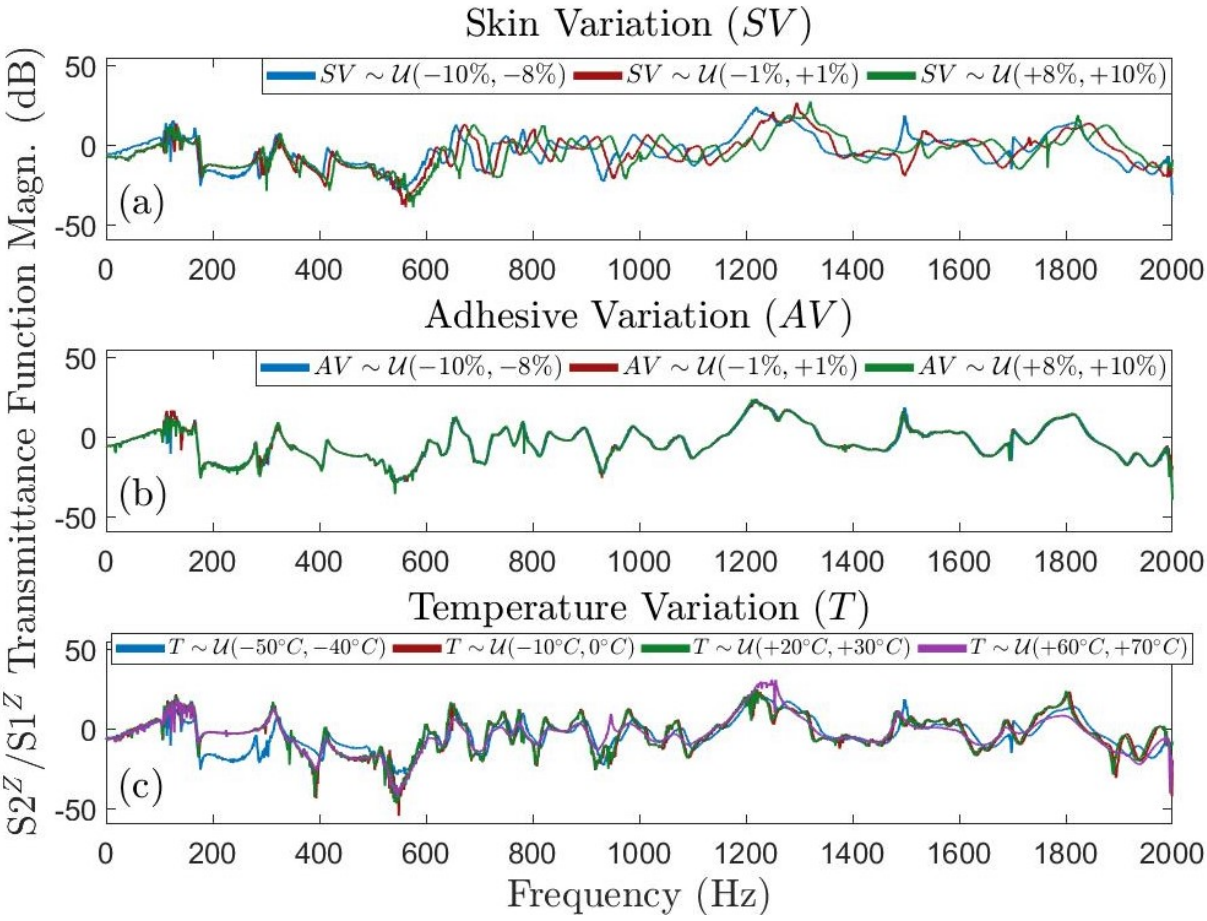

Figure 2: Isolated effects of each uncertainty factor (the rest maintained at their nominal values) on Welch-based MISO-TF $S2^Z/S1^Z$ magnitude estimates for the healthy aerostructures: (a) Skin variation effects (3 curves); (b) adhesive variation effects (3 curves); (c) temperature variation effects (4 curves). (Each uncertainty factor value sampled from each one of the indicated uniform distributions.)

EOC uncertainty is related to temperature, which affects the material properties, and the random force excitation profile. Temperature effects within the $-50\,^{\circ}$C to $70\,^{\circ}$C range are modeled via proper (quadratic) dependence of E11, E22, G12, and damping ζ. Two distinct force excitation profiles, referred to as P1 and P2, are employed, with P1 being a band-limited white noise and P2 a colored noise (obtained via an AutoRegressive model of order 6); further details are provided in [7].

The isolated effects of each one of the three first uncertainty factors on Welch-based TF estimates of the nominal Healthy aerostructure are presented in Figure 2; note that due to the use of the MISO-TF the force excitation profile effects are theoretically nonexistent and practically negligible. Evidently, the effects of SV are most pronounced, followed by those of temperature; yet those of the AV are quite negligible.

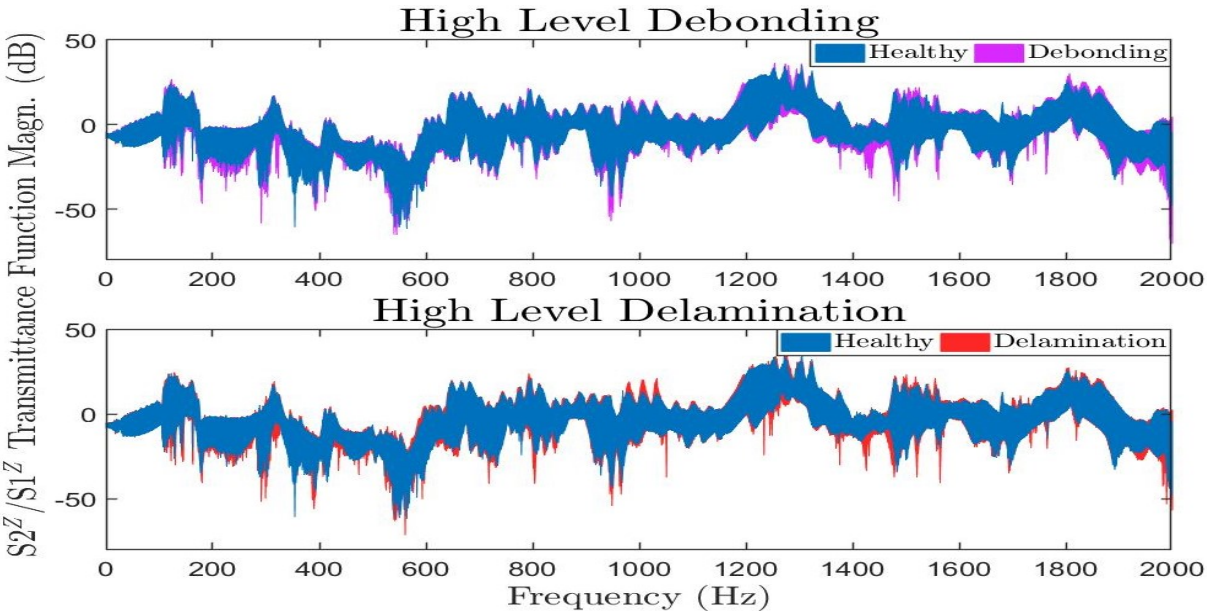

Figure 3: Effects of 'high' level debonding (upper plot) and delamination (lower plot), with damage locations being considered, on Welch-based MISO-TF $S2^Z/S1^Z$ magnitude estimates in the presence of all four uncertainty factors. (In each plot the curves corresponding to 9 Healthy structures under each one of 12 temperatures are shown in blue, along with those corresponding to 18 Damaged structures, each one under one of each of 10 temperatures under profile P1 and under one of 5 temperatures under profile P2.)

2.3 The damage scenarios

The damage types being considered are delamination (DL) and debonding (DB). Delamination occurs when laminas separate due to interlaminar (matrix) cracks, resulting into a reduction in stiffness within the affected area. In the present study the effect of delamination is modeled via degradation of material properties in a rectangular 20×20 mm area for 'low' level delamination and 50×50 mm for 'high' level delamination. Debonding, on the other hand, refers to insufficient adhesive material, which results in the separation of the adhered parts and is modelled via severe degradation of material properties and nullification of the mass density in the damaged area (10×20 mm and 10×50 mm corresponding to 'low' and 'high' debonding, respectively). Details are provided in Table 1.

Delamination damage on the skin and debonding on the adhesive layer are modeled at two distinct locations, D1 and D2, on the aerostructure (Figure 1; notice that the damage is on the YZ plane, which explains the previously noted acceleration measurement along the X axis). Combined with the 2 types of damage (DL/DB) and the two levels for each, 8 damage scenarios are obtained. The effects of 'high' level delamination (DL) and debonding (DB) at both locations, under uncertainty, on the Welch-based MISO-TF estimates are contrasted to those of the Healthy state, also under uncertainty, in Figure 3. Evidently, both damage scenarios have only subtle effects on the TF dynamics, a fact rendering damage diagnosis challenging.

3 OVERVIEW OF THE ROBUST RESPONSE-ONLY DAMAGE DIAGNOSIS METHODS

Damage diagnosis is based on the structural dynamics as reflected in a selected Multiple-Input Single-Output Transmittance Function (MISO-TF). This represents the relationship among m measured response signals, with $m-1$ of them acting as pseudo-inputs and the m-th as output. For this purpose an AutoRegressive with eXogenous excitation (ARX) model of orders n, n - that is an ARX(n, n) model of common AutoRegressive AR and eXogenous (X) orders - is employed:

$$y_m[t] + \sum_{i=1}^{n} a_i \cdot y_m[t-i] = \sum_{j=1}^{m-1} \sum_{i=1}^{n} b_i^j \cdot y_j[t-i] + w[t] \qquad w[t] \sim \text{i.i.d. } \mathcal{N}(0, \sigma_w^2) \tag{1}$$

with a_i $(i \in [1, n])$, b_i^j $(i \in [1, n],\ j \in [1, m-1])$ designating its AR and X parameters, respectively, and $w[t]$ an independent (white) Gaussian signal, with i.i.d. standing for identically independently distributed, while $\mathcal{N}(0, \sigma_w^2)$ stands for normal (Gaussian) distribution with zero mean and variance σ_w^2. Model order (n) selection and model parameter estimation for the ARX parameter vector:

$$\boldsymbol{\theta} := [a_1 \dots a_n \vdots b_1^1 \dots b_n^1 \vdots \dots \vdots b_1^{m-1} \dots b_n^{m-1}]^T \tag{2}$$

(^{T} designating transposition) and the variance σ_w^2 are based on standard identification procedures using available m-tuples of signals (signal sets) $(y_1[t], \dots, y_m[t])$ $(t \in [1, N])$ [11]. It is stressed that the use of MISO-TF model is instrumental in eliminating the effects of excitation profile uncertainty on the observed TF dynamics, and for this to happen the number $m-1$ of pseudo-input needs to be equal to the number of independent excitations acting on the structure.

Damage detection is formulated within a feature space which is based on a Principal Component Analysis (PCA) transformed and dimensionality reduced version of the original ARX model parameter vector $\boldsymbol{\theta}$ (details in [9]). Dimensionality reduction is based on retaining those Principal Components that collectively explain a *minor* portion of the feature vector variability, while dropping those that explain the major portion. The premise on which this is based is the expectation that the retained PCs are, evidently, less affected by uncertainty, hence the damage effects may be more evident in the (transformed and reduced) feature vector corresponding to them. It is yet noted that the original feature space, without transformation and dimensionality reduction, is employed for damage characterization.

The sample covariance matrix of the original feature that is employed in setting up the PCA is based on the parameter vector[1] $\widehat{\boldsymbol{\theta}}_k$ $(k \in [1, p])$ estimates obtained from p signal sets (m-tuples) $(y_1[t], \dots, y_m[t])$ $(t \in [1, N])$, each one corresponding to a distinct sample healthy structure available in the methods' Baseline/Training Phase. Further information on the detection and damage characterization methods are provided below.

3.1 Damage detection

Damage detection is pursued via two methods that may be viewed as providing proper approximations of the Healthy Subspace, defined as the part of the (transformed and reduced) feature space within which the healthy structures reside under uncertainty. The first method

[1]The hat designates estimate.

uses a Multiple Model (MM) [9] representation of the Healthy Subspace, while the latter uses a Hyper-Sphere (HS) type approximation [10]. Both approximations are established in the **Baseline/Training Phase** using the p available m-tuples of signals obtained from p structures and uncertainty combinations.

In the **Inspection Phase**, once a fresh m-tuple of signals (signal set) is obtained from a structure under unknown health state, a corresponding TF-ARX model of the same structure (model orders) employed in the Baseline Phase is estimated and its ARX parameter vector is transformed and truncated using the exact same PCs and procedure of the Baseline Phase. Damage detection is then carried out by computing a proper (pseudo) distance metric between the Healthy Subspace and the current model. If this is smaller than a user selected threshold the current structure is declared as healthy, else as damaged.

3.2 Hierarchical damage characterization

Hierarchical damage characterization is based on a procedure similar to that of the MM based damage detection method, but without feature vector transformation and dimensionality reduction. Hence damage characterization is based on the original feature space spanned by the ARX parameter vector. It is, of course, activated only in case the current structure is detected as damaged. A main difference in damage characterization is that it is supervised and hierarchical, meaning that signal sets from all possible damage states (damage type/location/level) are employed in the **Baseline/Training Phase**. Based on them, distinct MM-type damage subspaces are constructed: First DL-Delamination and DB-Debonding (irrespectively of location or level) subspaces are constructed, then DL/DB with location (D1 and D2) subspaces are constructed as DL-D1, DL-D2, DB-D1, DB-D2 (irrespectively of damage level). Finally, DL/DB and location (D1/D2) and damage level (H/L) subspaces are constructed as DL-D1-H, DL-D1-L, DL-D2-H, DL-D2-L, DB-D1-H, DB-D1-L, DB-D2-H, DB-D2-L.

In the **Inspection Phase** the procedure is as in damage detection, in that the current TF-ARX model obtained from a fresh m-tuple of signals (signal set) is employed. Hierarchical damage characterization is then based upon considering whether the current damage is classified as DL-Delamination or DB-Debonding (Stage 1). Once this is decided, damage location (D1 or D2) characterization is performed (two-class classification). Following this, a final two-class classification, as L-Low or H-High damage level, is performed. In contrast to damage detection, characterization is based on *cosine similarity*. This effectively means that an angular distance between the current structure and that of each considered subspace is computed, and the current structure is classified as belonging to that subspace with which the angular distance is minimal.

4 PERFORMANCE ASSESSMENT VIA NUMERICAL MONTE CARLO EXPERIMENTS

4.1 Preliminaries

As previously mentioned, a triplet of signals $(y_1[t], y_2[t], y_3[t])$ $(t \in [1, N];\ N = 10\,000)$ is employed in each numerical experiment as the number of acting excitations on the structure is two (Figure 1). The TF-ARX identification procedure applied on the healthy aerostructure under nominal conditions leads to an ARX$(135, 135)$ model with $\mathrm{S2}^Z$ acting as an output and $\mathrm{S1}^Z$,$\mathrm{S3}^Z$ as pseudo-inputs.

Structural State	No. of Structures (SV×AV)	No. of Temperatures under excitation P1/P2	Total No. of Experiments under P1/P2
Baseline (Learning) Phase			
Healthy	9	12/0 $\subseteq T_I$	108/0
Inspection (Diagnosis) Phase			
Healthy (H)	9	10/5 $\subseteq T_{II}$	90/45
Damage D$\mathbf{WD}^*_{\mathbf{Le}}$	9$^\diamond$	10/5 $\subseteq T_{II}$	90/45

*Type: **W**= B (Debonding) or L (Delamination); Location: **D**=D1 or D2; Level: **Le**= L (Low) or H (High).
No. of Damage Scenarios 8; Total No. of Experiments 135 (Healthy State) and 1 080 (Damage);
$^\diamond$Distinct structures per damage type (total 72).

Signal details: $f_s = 4$ kHz; $N = 10\,000$ samples ($2.5s$); Bandwidth (BWD) $0 - 2$ kHz; Mode Superposition integration: all modes in $[0 - 2]$ kHz; $f_{int} = 40$ kHz; Integration time step (constant): 2.5×10^{-4} s; No. of integration points 100 000

Table 3: Details on the Monte Carlo experiments.

4.2 Damage detection performance assessment

For the Baseline/Training Phase of the methods 9 structures are employed, obtained by sampling 3 SVs (common for skin E11, E22, G12) from each one of three uniform distributions of Figure 2, then having each sampled SV combined with three sampled AVs (for adhesive G12; the 1st from 1st uniform distribution, the 2nd from the 2nd, and the 3rd from the 3rd; also see Table 2). Each of the obtained 9 aerostructures is operating under 12 randomly selected temperatures from the temperature set T_I (one from each uniform distribution therein) and under the P1 excitation profile. This results into a total of 108 Baseline Experiments and a corresponding number of TF-ARX models (Table 3). Based on the corresponding sample covariance, the original feature space, of dimensionality 405, is PCA transformed and reduced into a dimensionality of 38 and 42 by retaining the last 38 and 42 PCs for the MM and HS methods, respectively.

For the Inspection Phase 9 distinct (different from those of the Baseline/Training Phase but determined via a similar procedure) aerostructures are employed, each one operating under 10 randomly selected temperatures from the temperature set T_{II} (one from each uniform distribution therein) and the P1 excitation profile. Also under 5 randomly selected temperatures from the temperature set T_{II} (one from 1st, 3rd, 5th, 7th and 9th uniform distribution) and the P2 excitation profile. This leads to a total of 135 signal triplets per each health state (90 under T_{II}, P1 and 45 under T_{II}, P2). As the healthy state and 8 damage scenarios are considered, assessment is based on 1 215 Inspection Experiments (135 Healthy and 1 080 Damaged; Table 3).

Damage detection performance is assessed via Accuracy, defined as the correct decision divided by the number of experiments (correct decision rate) and obtained for each one of the 8 damage scenario. It is noted that positive refers to the damaged state and negative to the healthy state, while the decision threshold used is the optimal for each damage scenario obtained from the corresponding Receiver Operating Characteristic (ROC) curve by selecting the point that minimizes the distance from the $(0, 1)$ corner.

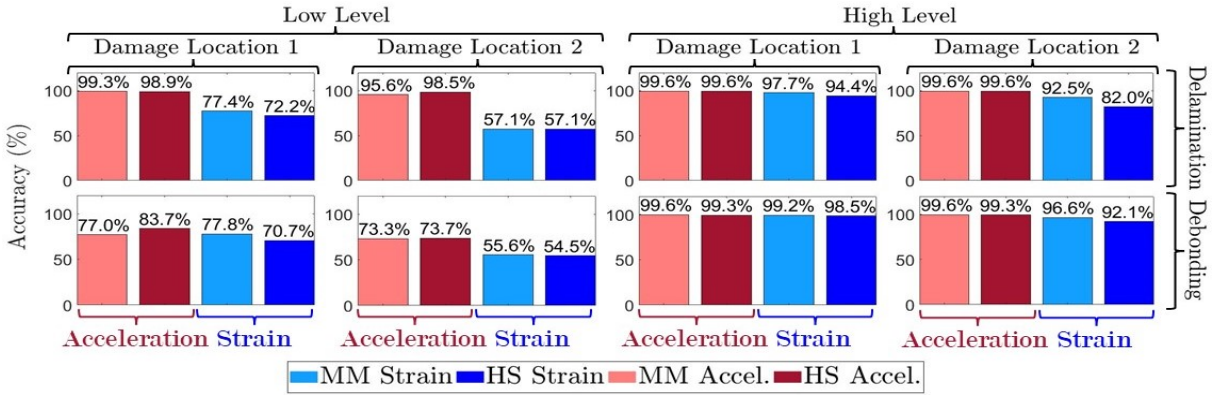

Figure 4: Damage detection performance assessment: Accuracy values for low/high (left/right column dyad) level delamination/debonding (upper/lower row) via strain (blue tints) and acceleration (red tints) signals by the MM and HS based methods (135 Inspection Experiments under both excitation profiles per damage scenario).

The damage detection assessment results are, for each damage scenario and both the MM and HS methods, presented in Figure 4 (blue tints). For purposes of comparison, corresponding acceleration-based results (obtained from our companion paper [7] using the exact same signal records and procedures) are also presented (red tints). It is observed, the strain-based detection performance is good for the 'high' level damage scenarios, but not as good for their 'low' level counterparts. The acceleration-based results are, almost uniformly, better, especially for the 'low' level damage scenarios, while the MM and HS methods achieve largely similar performance.

4.3 Damage characterization performance assessment

In order to ensure consistency and statistical reliability, a 'rotation' procedure is employed in this case. In each 'rotation' 45 out of 90 signal triplets under excitation profile P1 are selected for the Baseline/Training Phase for each damage scenario. The remaining (45) signal triplets are employed in the Inspection Phase, along with all signal triplets obtained under the P2 excitation profile (in total 90 signal triplets). Characterization results for the first stage of the hierarchical procedure are based on 72 000 Inspection Experiments (90 signal triplets $\times$ 8 considered damage scenarios $\times$ 100 rotations). This number decreases in subsequent stages as only correctly characterized Inspection Experiments are then considered.

The obtained results are presented in Figure 5, where the True Positive Rate (TPR; that is correct classification rate) is depicted (blue bars). Again, for purposes of comparison, corresponding acceleration based results from our companion paper [7] are also shown (red bars). As may be observed, the TPR for stage 1 exceeds 50%, indicating weak characterization of the damage type (debonding/delamination). This improves to over 60% for stage 2 (damage localization) and stage 3 (damage level characterization). The corresponding acceleration-based results are uniformly considerably better, remaining above 80% in all stages.

5 CONCLUDING REMARKS

The main conclusions drawn from this study, may be summarized as follows:

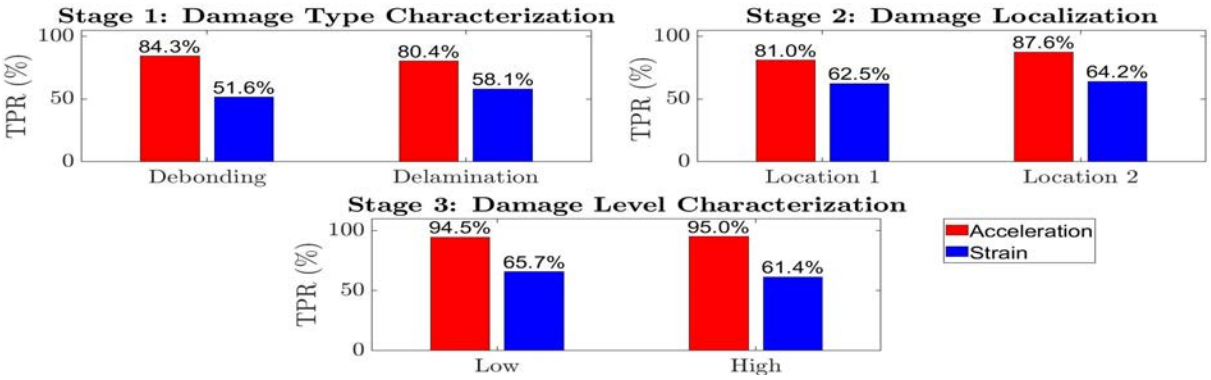

Figure 5: Hierarchical damage characterization assessment: Correct characterization rates for debonding/delamination (upper left plot), damage localization (upper right plot), and damage level (lower plot) via strain (blue) and acceleration (red) signals. (Stage 1 characterization assessment based on 72 000 Inspection Experiments.)

(i) Robust damage diagnosis, including detection as well as type, location, and size characterization based on dynamic *strain* signals has been shown to be effective for a population of 90 (18 Healthy and 9 from each of 8 Damage scenarios) composite structures and for both 'small' debonding and delamination damages.

(ii) The achievable strain-based damage detection accuracy may be as high as 99.2% for 'high' level damage and 77.8% for 'low' level damage (see Figure 4). The MM and HS detection methods performance is largely on par. Damage type (debonding/delamination) characterization performance is weak, but somewhat improved for damage localization and damage level characterization.

(iii) Comparing strain-based to acceleration-based damage diagnosis, the latter achieves higher marks, especially for 'low' level damage detection and all stages of damage characterization (for 'higher' level damage the diagnostic performance is largely similar; see our experimental parallel study [8]). Yet, strain-based SHM may be still useful; perhaps in combination with its acceleration-based counterpart. This is an area of current investigation.

Acknowledgements

The study has been carried out within the framework of the research project 'Robust to Uncertainty Machine Learning Based Structural Health Monitoring for a Population of Nominally Identical Composite Aerostructures - REALISM' (project code: T10DIS-00050, MIS 5074648) which is realized within the context of the 'Bilateral and multilateral R&T cooperation between Greece and Israel' and is co–financed by the European Regional Development Fund (ERDF) of the European Union and Greek national funds through the Operational Program Competitiveness, Entrepreneurship, and Innovation (EPAnEk).

References

[1] P. Capoluongo, C. Ambrosino, S. Campopiano, A. Cutolo, M. Giordano, I. Bovio, L. Lecce, and A. Cusano, "Modal analysis and damage detection by Fiber Bragg grating sensors,"

Sensors and Actuators A: Physical, vol. 133, no. 2, pp. 415–424, 2007.

[2] X. Li, L. Wang, S. Law, and Z. Nie, "Covariance of dynamic strain responses for structural damage detection," *Mechanical Systems and Signal Processing*, vol. 95, pp. 90–105, Oct. 2017.

[3] S. Sharma, S. K. Dangi, S. K. Bairwa, and S. Sen, "Comparative study on sensitivity of acceleration and strain responses for bridge health monitoring," *Journal of Structural Integrity and Maintenance*, vol. 7, no. 4, pp. 238–251, Oct. 2022.

[4] T. Loutas, A. Panopoulou, D. Roulias, and V. Kostopoulos, "Intelligent health monitoring of aerospace composite structures based on dynamic strain measurements," *Expert Systems with Applications*, vol. 39, no. 9, pp. 8412–8422, Jul. 2012.

[5] M. Lin, S. Guo, S. He, W. Li, and D. Yang, "Structure health monitoring of a composite wing based on flight load and strain data using deep learning method," *Composite Structures*, vol. 286, no. 115305, Apr. 2022.

[6] J. Alvarez-Montoya, A. Carvajal-Castrillón, and J. Sierra-Pérez, "In-flight and wireless damage detection in a UAV composite wing using fiber optic sensors and strain field pattern recognition," *Mechanical Systems and Signal Processing*, vol. 136, no. 106526, Feb. 2020.

[7] I. E. Saramantas, P. E. Konis, I. M. Kriatsiotis, Y. Ofir, I. Kressel, P. E. Spiliotopoulos, F. Fera, J. S. Sakellariou, S. D. Fassois, N. Galiatsatos, F. Giannopoulos, C. Spandonidis, M. Tur, and Z. Tzioridis, "An exploratory study on data-driven vibration based damage detection and characterization for a population of composite aerostructures," *Proceedings of the XII International Conference on Structural Dynamics (EURODYN2023)*, 2023.

[8] F. T. Fera, P. E. Spiliotopoulos, I. E. Saramantas, Y. Ofir, I. Kressel, S. D. Fassois, J. S. Sakellariou, M. Tur, and C. Spandonidis, "Dynamic strain versus acceleration based robust structural health monitoring for a group of composite aerostructures: experimental assessment," *Proceedings of the X ECCOMAS Thematic Conference on Smart Structures and Materials (SMART 2023)*, 2023.

[9] K. Vamvoudakis-Stefanou, J. Sakellariou, and S. Fassois, "Vibration-based damage detection for a population of nominally identical structures: Unsupervised Multiple Model (MM) statistical time series type methods," *Mechanical Systems and Signal Processing*, vol. 111, pp. 149–171, Oct. 2018.

[10] K. Vamvoudakis-Stefanou, S. Fassois, and J. Sakellariou, "An automated hypersphere-based healthy subspace method for robust and unsupervised damage detection via random vibration response signals," *Structural Health Monitoring*, vol. 21, no. 2, pp. 465–484, Mar. 2022.

[11] L. Ljung, *System Identification: Theory for the User (2nd ed.)*. Upper Saddle River, NJ 07458: Prentice Hall PTR, 1999.